PAPER

Check for updates

A new 3D crosslinked polymer strategy for highly efficient oxygen reduction Fe–N$_x$/C catalysts†

Zonggui Shao,[ab] Lei Tong,[ab] Yasheng Qian,[ab] Rongmin Dun[ab] and Wenmu Li [ID] *[a]

The development of non-precious metal (NPM) catalysts with superior performance to replace Pt/C is critical for the wide application of proton-exchange membrane fuel cells. In this work, a three-dimensional crosslinked polymer with highly dispersed iron–nitrogen (Fe–N) coordination units and a mechanically robust framework is designed, synthesized and used as the sole precursor to obtain Fe-coordinated nitrogen-doped carbon (Fe–N$_x$/C) oxygen reduction reaction (ORR) catalysts. After optimization of the pyrolysis conditions and the use of SiO$_2$ templates to modify the catalyst nanostructure, a highly active catalyst of T-FeNC-800R is obtained, which exhibits a high half-wave potential of 751 mV in 0.1 M HClO$_4$. Besides, the T-FeNC-800R catalyst has an excellent ORR activity with onset and half-wave potentials of 1030 and 873 mV in 0.1 M KOH, respectively, which are higher than those of Pt/C (onset and half-wave potentials are 1009 and 855 mV *vs.* RHE, respectively). Moreover, this catalyst exhibits an almost four electron transfer process, high long-term stability, and better methanol tolerance than Pt/C catalyst in acidic media. The excellent oxygen reduction reaction performance of T-FeNC-800R can be attributed to the mesoporous structure, high specific surface area and a large number of exposed active sites. Moreover, the effects of the SiO$_2$ template, secondary pyrolysis and iron element on the catalytic performance are systematically discussed.

Introduction

Polymer electrolyte membrane fuel cells (PEMFCs) are considered as one of the most promising new energy systems for future stationary and mobile power generation due to their high energy density, high efficiency and zero emissions.[1–4] However, the cathode suffers from relatively sluggish ORR kinetics and therefore high overpotential, which limits the performance of PEMFCs.[5] To date, platinum (Pt) or Pt-based catalysts are widely used for cathodic materials owing to having the best catalytic activity for ORR.[6] Unfortunately, the prohibitively high cost, poor stability and serious intermediate intolerance, such as CO poisoning and methanol crossover, severely hinders the practical use of PEMFCs.[7,8] Therefore, great efforts have been directly devoted to searching for alternative non-precious metals or even metal-free species catalysts to substitute the Pt-based catalysts over the past decades.[9–12] Among them, the iron-based (Fe-based) catalysts were regarded as a promising alternative to Pt-based catalysts for the ORR.[13–16]

Although the significant progresses have been persistently achieved in Fe-based electrocatalysts, the inefficiently traditional trial and error experiment approach was still the main ways for the R&D of Fe-based catalysts.[8,17] This is because most of high performance Fe-based catalysts obtained were subjected to high temperature pyrolysis, making them extremely difficult to tailor the structure and surface properties, letting alone the identification of the nature of Fe-based catalysts active sites.[18] Quite recently, a number of studies have been focused on the identification of the active sites structure of Fe-based catalysts. Although further confirmation is needed, it is reported that the highly plausible active site structures of Fe-based catalysts was the iron ions attaching to the carbon through coordinating with nitrogen moieties.[19–22] One possible method to resolve these challenges is to synthesize a novel precursor with a high content of thermally stable nitrogen, and with a structure that can readily coordinate with iron, generating well-distributed Fe-coordinated nitrogen (Fe–N$_x$) sites prior to pyrolysis. Besides purposely selecting and designing precursors containing large numbers of potential active sites, the optimization of catalyst nanostructure is also critical to obtain highly ORR active Fe–N$_x$/C catalysts. Efficient ORR can be only achieved by continuously transferring protons, oxygen molecules and electrons to active sites through the favorable percolation networks.[23] Herein, the suitable mesoporous structure and high conductivity properties are of significance for their high performance Fe-based catalysts.[24] Besides, the mesoporous structure is also helpful to increase the specific surface area of the catalyst and make the active sites accessible to reactants.[25,26]

[a]Key Laboratory of Optoelectronic Materials Chemistry and Physics, Fujian Institute of Research on the Structure of Matter, Chinese Academy of Sciences, Fuzhou 350002, P. R. China. E-mail: liwm@fjirsm.ac.cn

[b]University of Chinese Academy of Sciences, Beijing 100049, China

In this work, a three-dimensional crosslinked polymer was designed, synthesized and used as the solely precursor. This polymer consists of alternating rigid aromatic imide segments and triphenanthroline-coordinated ferrous ions. The high carbon residue aromatic polyimides are deliberately utilized to keeping all ferrous ions well separated initially, which could effectively prevent ferrous ions form sintering during pyrolysis even under high initial iron content and thus create high active sites density Fe-based catalysts.[27–30] In order to further enhance the ORR performance of Fe-based catalysts, SiO_2 nanoparticles was introduced as a template to create more favorable mesoporous structure and percolation properties. Highly active mesoporous ORR catalysts were successfully prepared and the influencing factors of catalyst performance were systematically discussed.

Experimental

Synthesis of catalysts

The $FeBr_2$ (98%), 2,2′-bis-(3,4-dicarboxyphenyl) hexafluoropropane dianhydride (6FDA) (98%) and 20 wt% Pt/C were purchased from Alfa Aesar (China) Chemical Co., Ltd. (Shanghai, China); the 1,10-phenanthroline monohydrate (99%) was purchased from Sinopharm Chemical Reagent Co., Ltd. (Shanghai, China) and used without further purification. The 5-nitro-1,10-phenanthroline and 5-amino-1,10-phenanthroline were prepared according to the reported literature.[31,32] The bisPhen/6FDA was obtained from the 5-amino-1,10-phenanthroline and 6FDA and the structure of bisPhen/6FDA was verified by H1 NMR (Fig. S1 and S2†).[33] The mixture of 15 and 50 nm silicon spheres at the rate of 1 : 1 in mass were used for hard template (SiO_2). The catalysts were prepared by homogeneously dispersing iron and bisPhen/6FDA precursors onto the surface of SiO_2. In a typical synthesis process as shown in Scheme 1, 240 mg (0.3 mmol) bisPhen/6FDA was dissolved in 5 mL DMF and 720 mg of SiO_2 was added under magnetic stirring. Then 1 mL DMF solution containing 43 mg (0.2 mmol) $FeBr_2$ was added under stirring conditions, the reaction mixture was heated to 80 °C and was stirred for 1 h. A gel was obtained after cooling and this gel was scraped into water then was crushed,

the precipitate was filtered off and washed with water and methanol, then drying under a vacuum at 85 °C for 6 hours. The resulting solid was heat treated under nitrogen at 800 °C for 2 h with temperature ramp rates of 10 °C min^{-1}. Finally, the SiO_2 was leached out using excess amounts of 40 wt% hydrofluoric acid (HF) to obtain the T-FeNC-800 catalyst. The T-FeNC-800 catalyst was re-pyrolyzed at 900 °C for 3 hours under a nitrogen atmosphere to form the T-FeNC-800R catalyst (Fig. S4†). The detailed synthesis parameters for each sample prepared in this work was listed in Table S1.†

Sample characterization

The proton nuclear magnetic resonance (1H NMR) spectra was recorded on a 400 MHz spectrometer. The thermogravimetric (TG) analysis of Fe-bisPhen/6FDA and Fe-phenanthroline was carried out in a range from 30–1000 °C under nitrogen atmosphere with a heating rate of 10 °C min^{-1}. Transmission election microscopy (TEM) was performed using a JEM-2010 (JEOL Ltd, Japan) operating at 200 kV. The Brunauer–Emmett–Teller (BET) method was used to determine the specific surface area by measuring the adsorption of N_2 using an ASAP2020 volumetric adsorption analyzer (Micromeritics, U.S.A.). The specific surface area was determined by the standard BET method in a relative pressure range of 0.05–0.2, the pore size distribution curves of micropores and mesopores was calculated by the Horvath–Kawazoe (HK) method and by the Barrett–Joyner–Halenda (BJH) method, respectively. Before measurements, all samples were degassed at 120 °C for at least 10 h. Raman spectra was collected on a LabRAM HR (Horiba Jobin Yvon, Ltd., France) with a 532 nm laser excitation. Surface analysis of the catalyst particles was carried out using an XPS on a VG Scientific ESCALAB MK II using Al Kα radiation (1486.71 eV) and the C 1s peak at 284.8 eV as the internal standard. Powder X-ray diffraction (XRD) patterns were performed with a MiniFlex-II diffractometer (Rigaku, Japan) using a Cu Kα radiation source.

Electrochemical measurements

For rotating disk electrode (RDE) and rotating ring disk electrode (RRDE) measurements, catalyst ink was prepared by sonicating 4 mg of catalyst in 985 μL of ethanol and 38 μL of 5 wt% Nafion solution for 60 min. Then, 20 μL of ink was deposited on the rotating disk electrode (RDE, 5 mm diameter, 0.196 cm^2 geometric surface areas) and 25 μL of ink was deposited on the rotating ring-disk electrode (RRDE, E7R9, disk area: 0.2475 cm^2, Pt ring area: 0.1866 cm^2), respectively. The catalyst loading on RDE or RRDE was 0.4 mg cm^{-2}. Commercially available Pt/C catalyst (Alfa Aesar, 20 wt% Pt) was measured for comparison. 4 mg Pt/C was dispersed in 2 mL ethanol and 38 μL of 5 wt% Nafion solution and then sonicated for 60 min, and the ink was drop coated onto the glassy carbon disk of RDE (10 μL) and RRDE (12.5 μL). The Pt/C catalyst loading on RDE or RRDE was 20 μg Pt cm^{-2}. A conventional three-electrode cell was employed incorporating an Ag/AgCl as the reference electrode, a Pt wire as the counter electrode and the RDE or RRDE as the working electrode, the electrolyte was 0.1 M $HClO_4$ solution. In all test results, the potentials were
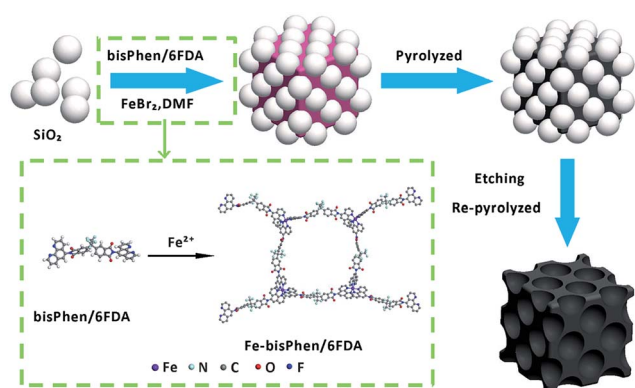
Scheme 1 The schematic illustration of the synthesis of mesoporous FeNC catalyst.

converted to values *versus* the reversible hydrogen electrode (RHE). The conversion from Ag/AgCl to RHE is done by measuring the voltage ΔE between the Ag/AgCl and a Pt-black coated Pt wire immersed in 0.1 M $HClO_4$ or 0.1 M KOH saturated with H_2, the measured ΔE was 0.267 V in 0.1 M $HClO_4$ and 0.94 V in 0.1 M KOH, respectively (Fig. S5 and S6†). LSV measurements were carried out in N_2- or O_2-saturated 0.1 $HClO_4$ or 0.1 M KOH solution, at a scan rate of 10 mV s^{-1}. LSV measurements in the RRDE were carried out in N_2- or O_2-saturated 0.1 $HClO_4$ solution at a scan rate of 10 mV s^{-1} also, a potential of the Pt ring disk was set to 1.2 V *vs.* RHE. Before each measurement, the solution was bubbled with N_2 or O_2 gas for 30 min, and the working electrode was activated by sweeping between 0.2 and 1.4 V at a scan rate of 50 mV s^{-1} for 10 min. Corrected oxygen reduction currents were obtained by subtracting the background current obtained for the N_2-saturated solution from the measured current obtained for the O_2-saturated solution. For the methanol crossover study, the current was recorded at 0.667 V *vs.* RHE with an RDE rotation rate of 900 rpm, with 1 M methanol being added into the O_2-saturated electrolyte around 300 s. The lifetime stability test was carried out with 10 000 cycles in the potential window of 0.6 to 1.0 V *vs.* RHE in O_2-saturated electrolyte with the scan rate of 50 mV s^{-1} on stationary electrode. After performing 10 000 stability test cycles, corresponding LSV was recorded to compare the final activity with initial activity of the samples. For this purpose, the $E_{1/2}$ before and after the stability test were compared. The hydrogen peroxide yield (H_2O_2 (%)) and the electron transfer number (n) calculated from the RRDE measurement was based on the disk current (I_D) and ring current (I_R) *via* the following equation:

$$H_2O_2 = \frac{2I_R}{N|I_D| + I_R} \times 100 \qquad (1)$$

$$n = 4 - \left(2\frac{H_2O_2(\%)}{100}\right) \qquad (2)$$

where $N = 0.37$ is the current collection efficiency of Pt ring.

Results and discussion

The T-FeNC-800R catalyst was synthesized by mixing the Fe-bisPhen/6FDA and spherical silica template in solution, followed by heat treating at 800 °C, hydrofluoric acid (HF) etching, and a second heat treating at 900 °C (Scheme 1). The microscopic structure of T-FeNC-800R was evaluated by transmission election microscopy (TEM) as shown in Fig. 1. Some disordered spherical mesopores were clearly observed in the T-FeNC-800R (Fig. 1b). This is a result of the vacation of silica during HF etching. As shown in Fig. 1c, most graphite nanosheets were crimped and arranged irregularly, suggesting the poor crystallization of the carbon frameworks in the resulting products. Furthermore, the selected-area electron diffraction (SAED) pattern in the Fig. 1d also confirmed the poor graphite crystallinity of T-FeNC-800R.[34]

In order to reveal the effect of secondary pyrolysis and silicon template on the activity of the catalyst, we also prepared FeNC-
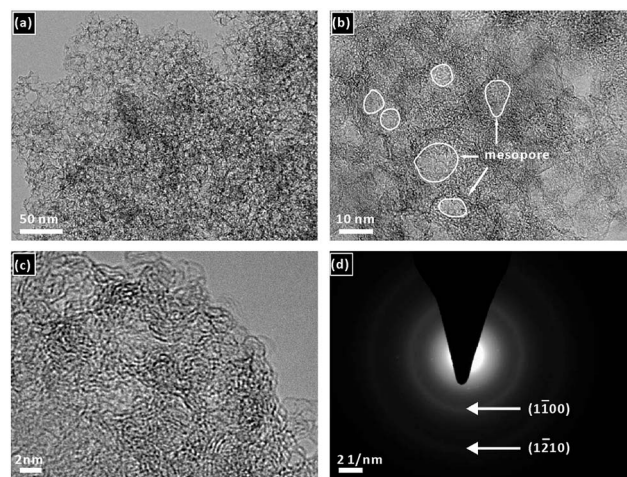

Fig. 1 (a) and (b) TEM and (c) HRTEM images of T-FeNC-800R; (d) the electron diffraction pattern of T-FeNC-800R.

800R (without template) and T-FeNC-800 (use template but undergoes only one pyrolysis at 800 °C). The X-ray diffraction (XRD) patterns and Raman spectroscopy were performed to determine the crystal structure of our catalysts (Fig. S7 and S8†). The peaks around $2\theta = 26°$ assigning to (002) diffraction peaks of graphitic carbons and the peak at 44° corresponding to (100) plane of graphitic carbon.[35] As shown in Fig. S7,† both catalysts (T-FeNC-800 and T-FeNC-800R) prepared with silicon template exhibited much lower intensity of (002) and (100) peaks than those of FeNC-800R prepared without template, which indicated that the introduction of silicon template can hinder the graphitization in the whole structure of the catalyst. Moreover, this conclusion can also be verified by the analysis of Raman spectroscopy. The ratio of the D and G band intensities (I_D/I_G) in Raman spectroscopy was often used to evaluating the degree of graphitization of carbon frameworks, the higher the ratio of I_D/I_G, the smaller the degree of graphitization.[36] As Fig. S8† showed, two prominent peaks corresponding to the D band (about 1360.0 cm^{-1}) and G band (about 1584.9 cm^{-1}) were observed in these samples. FeNC-800R (1.41) exhibited a much smaller I_D/I_G value than T-FeNC-800R (3.00) and T-FeNC-800 (3.13), which can jump to the same conclusion as that of XRD.

The nitrogen sorption measurements were performed to investigate the specific surface area and pore size of the catalysts. The N_2 adsorption/desorption isotherm and pore size distribution from the Barrett–Joyner–Halenda (BJH) model were shown in Fig. 2a and b, respectively. It's worth noting that FeNC-800R without any template display a near 390 m^2 g^{-1} high specific surface area. Meanwhile, the typical mesoporous property was also observed in FeNC-800R according to its feature of type IV isotherm (Fig. 2a).[37] In fact, this decent nanostructure of FeNC-800R can be solely attributed to the special structure of our designed precursor. On the one hand, the three-dimensional crosslinked polymer itself has the porous property. On the other hand, the trifluoromethyl groups in the structure of our precursor may decomposed at high temperature to form gas fluoride molecules thus to create more specific
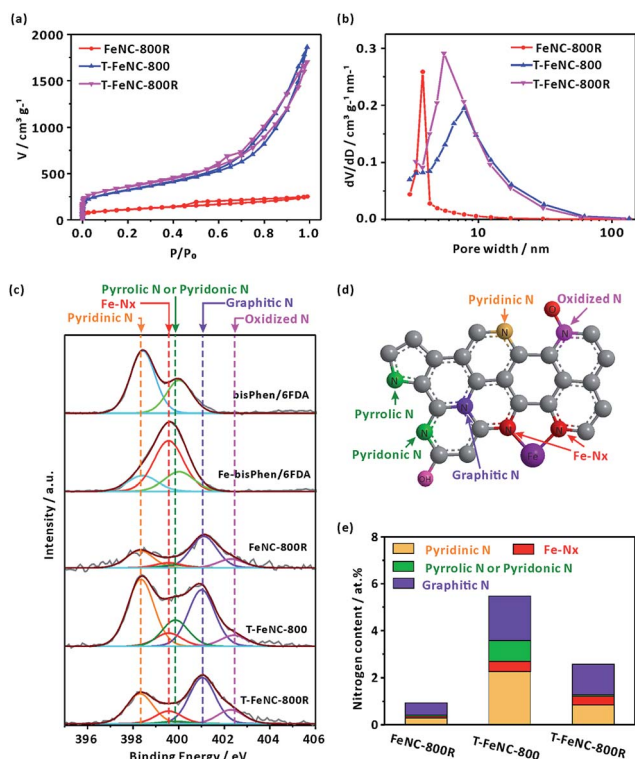
Fig. 2 (a) N_2 adsorption–desorption isotherms and (b) the pore size distribution of catalysts. (c) N 1s XPS spectra of different sample. (d) Schematic illustration of different nitrogen species. (e) Content of different N species in FeNC-800R, T-FeNC-800 and T-FeNC-800R.

surface area. However, both the drying procedure of precursor from a gel state to a powder state (Fig. S4†) and the subsequent pyrolysis treatment of the powder were suspected to break the pore structure of the precursor. This resulted in limiting the mesoporous volume ($0.357 \text{ cm}^3 \text{ g}^{-1}$) and distribution (average pore size of 3.82 nm) of FeNC-800R. Both T-FeNC-800 and T-FeNC-800R showed much more favorable nanostructure than that of FeNC-800R, which clearly demonstrated the positive effects of nano silica template. Although the mesoporous volume and pore size of T-FeNC-800R are slight lower relative to T-FeNC-800 (Table S2†), the microporous specific surface area and content of T-FeNC-800R increases after second pyrolysis. This is due to the partial collapsing of mesopores and the volatilization of some small molecules (such as C_xN_y, NO_x, CO_2, CH_x, etc.) during the second pyrolysis process.[38]

X-ray photoelectron spectroscopy (XPS) measurement was performed to analyze the elemental compositions of the catalysts (Table S3†). It's interesting that the nitrogen content of the FeNC-800R is as low as 1.09%, which is much lower than that of T-FeNC-800 (5.52%) and T-FeNC-800R (2.97%). There are a number of factors that should be responsible for this result, and the low porosity of FeNC-800R is the most important one, which can't expose enough specific surface area and nitrogen for the XPS detection. To further explore how the Fe-based preparing procedures affect the evolution of nitrogen, the high-resolution N 1s spectra of catalysts was performed. The bisPhen/6FDA and Fe-bisPhen/6FDA monomers were utilized as

model compounds to verify the binding energy of iron-nitrogen coordination (Fe–N_x). The N 1s curve of bisPhen/6FDA patently showed two peaks at 398.42 and 400.02 eV (Fig. 2c), which was ascribed to two distinct nitrogen bonding environments (Fig. S11a†). Accordingly, the N 1s curve of Fe-bisPhen/6FDA could be divided into three peaks at 398.42, 399.56 and 400.02 eV, which are assignable to three distinct nitrogen bonding environments (Fig. S11b†). By comparing the N 1s curve of bisPhen/6FDA and Fe-bisPhen/6FDA, the peak at 399.56 eV of Fe-bisPhen/6FDA could be safely assigned to the pyridinic nitrogens directly attaching to ferrous ions (Fe–N_x) (Fig. S11b†).[20] The high-resolution N 1s spectra of catalysts could be deconvoluted into five peaks, which corresponded to pyridinic N (398.30 eV), Fe–N_x (399.56 eV), pyrrolic N or pyridonic N (399.85 eV), graphitic N (401.03 eV) and oxidized N (402–403 eV), respectively (Fig. 2d).[12,28,39] All types nitrogen in T-FeNC-800R decreased comparing to those of T-FeNC-800 after the second pyrolysis (Fig. 2e). Especially, the signal assignable to pyrrolic N or pyridonic N of catalyst T-FeNC-800R was hardly observed. Two peaks 710.9 and 713.2 eV assignable to the N-coordinated Fe^{2+} and Fe^{3+} species were also observed in the corresponding Fe 2p XPS spectra (Fig. S12†), which clearly showed the presence of Fe in the catalysts.[40]

The ORR activity of prepared catalysts was assessed using rotating disk electrode (RDE) in 0.1 M $HClO_4$ solution. The optimum pyrolysis condition for ORR activity was studied by only changing pyrolysis temperatures, SiO_2 template, and second pyrolysis at 900 °C. The best ORR Fe-based catalysts were realized at the first pyrolysis temperature of 800 °C and the second pyrolysis temperature of 900 °C (Fig. S13†). The structure feature of the precursor made FeNC-800R exhibit the characteristic of mesoporous materials, but the limited percolation channels which is not favor in increasing its ORR activity ($E_{1/2} = 624$ mV vs. RHE) (Fig. 3a). As Fig. 3a showed, the ORR activity only enhance 4 mV from catalyst FeNC-800R to T-FeNC-800 after the introduction of silica template, though their BET surface area increase from FeNC-800R ($390 \text{ m}^2 \text{ g}^{-1}$) to T-FeNC-800 ($1135 \text{ m}^2 \text{ g}^{-1}$). This strongly indicated that the ORR activity of Fe-based catalysts could not be enhanced simply by increasing their surface area and the nitrogen content. To further improving the ORR activity of our Fe-based catalysts, the second pyrolysis procedure was introduced. The T-FeNC-800R exhibited a 123 mV half-wave potential increase to 751 mV vs. RHE comparing to T-FeNC-800, and only 31 mV negative than that of Pt/C ($E_{1/2} = 782$ mV vs. RHE). Moreover, when switching to the alkaline media, the $E_{1/2}$ and E_{onset} of T-FeNC-800R were 873 mV and 1030 mV, respectively, both of which higher than those of Pt/C ($E_{1/2} = 855$ mV and $E_{\text{onset}} = 1009$ mV vs. RHE) (Fig. 3a). This excellent result was also comparable to other non-precious catalysts (Table S4†). The significant improvement of the T-FeNC-800R's ORR activity may be attributed to the increasing of the density of highly active Fe–N_x sites and the purity of Fe-based catalyst. Although the exact chemical structure of Fe-based catalysts' active sites is still an unsolved puzzle, it's well document that highly active sites of Fe-based catalysts derived mainly from the micropores.[25,41,42] Indeed, the specific surface area of T-FeNC-800R's micropores are almost double
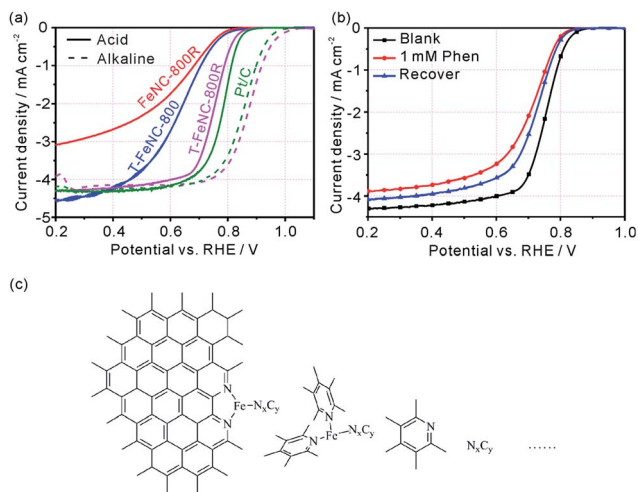
Fig. 3 (a) RDE results of FeNC-800R, T-FeNC-800, T-FeNC-800R and Pt/C in O_2-saturated 0.1 M $HClO_4$ (full line) and 0.1 M KOH (imaginary line) at 900 rpm with a scan rate of 10 mV s^{-1}. (b) RDE results (in O_2-saturated 0.1 M $HClO_4$ at 900 rpm, with a scan rate of 10 mV s^{-1}) of T-FeNC-800R (without and with 1,10-phenanthroline). (c) Schematic illustration of the highly active Fe–N_x/C species and possible nitrogen containing small fragments.

after second pyrolysis comparing to T-FeNC-800 (Table S2†), though the content of nitrogen assignable to the Fe–N_x decreased from 0.45% to 0.36% (Table S3†). The purity of Fe-based catalysts is also a key factor to affect their ORR activity. Our catalysts system should be very complicated since all of them resorted to high temperature pyrolysis. However, they should contain the highly active Fe–N_x/C species and the active N species at least (Fig. 3c). Some nitrogen active species may attach to a very small fragment of graphene sheet, which may be dissolvable in acid solution. These dissolvable nitrogen containing small fragments N_xC_y may further react with highly active Fe–N_x/C species and disable them to ORR under the acid leaching condition. To prove our assumption, 1,10-phenanthroline (Phen) was used as a model compound to test how the soluble nitrogen containing fragment affects the ORR activity of Fe-based catalysts. The Phen test was performed by the method of the LSV without and with adding 1 mM Phen to 0.1 M $HClO_4$. The $E_{1/2}$ of T-FeNC-800R catalyst negatively shifted by 43 mV after the adding of 1 mM Phen. However, the ORR activity of T-FeNC-800R didn't recovered even after the catalyst was multiply washed with de-ions water to remove Phen (Fig. 3b). This clearly demonstrated the destructive effect of nitrogen containing impurity for the ORR. The second pyrolysis which can remove ORR inactive impurities (C_xN_y, C–F, Fe–F, N–O, *etc.*), recover the possible Fe–N_x/C active sites, and clean the electrochemical interface leading to more ORR active sites, may contribute the increase of the ORR activity.[38,43] In fact, the almost disappearance of deconvolution signal assignable to the low or inactive pyrrolic and pyridonic N of T-FeNC-800R after the second pyrolysis (Fig. 2e),[12] clearly demonstrated the importance and necessity of second pyrolysis.

In order to further identify the true active species of our catalysts, the T-NC-800R catalyst without any iron ions was

prepared according to the same synthetic procedure of T-FeNC-800R. The ORR activity of T-NC-800R is much worse than that of T-FeNC-800R (Fig. 4a), though it possessed comparable high microporous specific surface areas and N content to the T-FeNC-800R (Tables S2 and S3†). The only different between the T-NC-800R and T-FeNC-800R is the possible highly active Fe–N_x species (Fig. 4b).

To confirm the importance of Fe–N_x species for the ORR, an electrochemical poisoning test by NaSCN was also conducted.[42–47] A sharp current density decrease was observed at 0.75 V after the adding 5 mM SCN$^-$ into the electrolyte (Fig. 4c). The corresponding LSV of T-FeNC-800R also exhibited a 95 mV $E_{1/2}$ negatively shift. Besides, almost complete ORR activity recovery was observed after the complete removing of SCN$^-$ ions (Fig. 4d). These results combined with XPS analysis strongly suggested that Fe–N_x species are the highly active sites in the Fe-based catalysts.

To better understand the electrochemical catalytic behavior of T-FeNC-800R, its Tafel slope was calculated (Fig. 5a). It's obvious that a similar Tafel slope was observed for T-FeNC-800R (54 mV per decade) and Pt/C (52 mV per decade). This means that the transfer of the first electron was probably the rate-determining step in ORR catalyzed by T-FeNC-800R, which is similar to platinum-based materials.[9] Furthermore, the H_2O_2 yield and electron transfer number (n) have also been calculated by results of RRDE test (the potential of the Pt ring electrode was set to 1.2 V *vs.* RHE). It could be seen from Fig. 5b that the peroxide species yield of T-FeNC-800R was less than 7.58% and the electron-transfer number (n) was higher than 3.85 in the measured potential range from 0.2 to 0.8 V, which is close to the value of Pt (2.35% and 3.96, respectively), suggesting the four
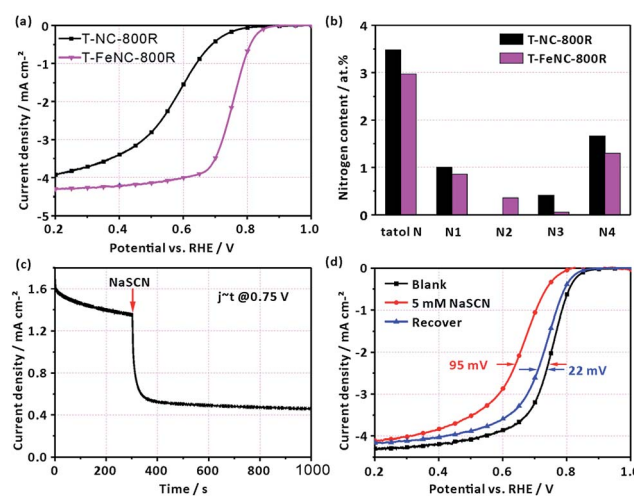
Fig. 4 (a) RDE results (in O_2-saturated 0.1 M $HClO_4$ at 900 rpm, with a scan rate of 10 mV s^{-1}) of T-NC-800R and T-FeNC-800R. (b) Content of total N, pyridinic N (N1), Fe–N_x (N2), pyrrolic N or pyridonic N (N3), graphitic N (N4) in T-NC-800R and T-FeNC-800R. (c) Current–time (I–t) curves of T-FeNC-800R on a rotating disk electrode (900 rpm) in O_2-saturated 0.1 M $HClO_4$ solution (without and with SCN$^-$). (d) RDE results (in O_2-saturated 0.1 M $HClO_4$ at 900 rpm, with a scan rate of 10 mV s^{-1}) of T-FeNC-800R (without and with SCN$^-$).
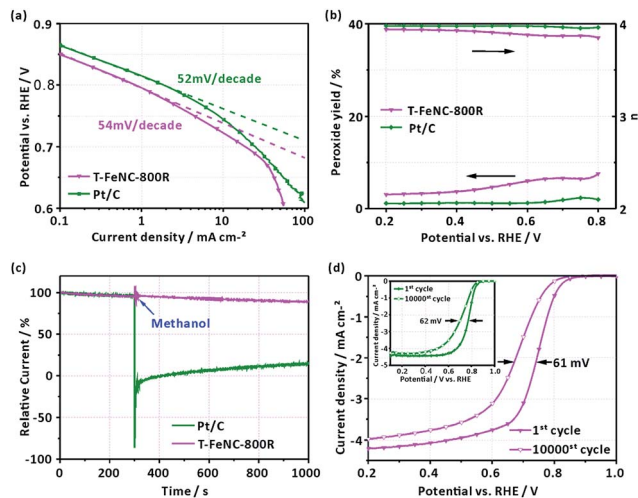
Fig. 5 (a) Tafel plots of T-FeNC-800R and Pt/C obtained from the RDE measurements. (b) H_2O_2 yield and electron-transfer number (n) of T-FeNC-800R and Pt/C. (c) Current–time (I–t) curves of T-FeNC-800R and Pt/C in O_2-saturated 0.1 M $HClO_4$ solution (without and with 1 M methanol). (d) LSV of T-FeNC-800R and Pt/C (inset) before and after 10 000 cycles in O_2-saturated 0.1 M $HClO_4$ solution. All tests on a rotating disk electrode (900 rpm) with a scan rate of 10 mV s^{-1}.

electron pathway of the ORR process for the T-FeNC-800R catalyst. The tolerance to methanol crossover and the stability of the catalyst material are also important parameters to be evaluated. The methanol-tolerance test was performed by the method of current–time (I–t) plots with adding 1 M methanol to 0.1 M $HClO_4$ after about 300 s (at a potential of 0.667 V $vs.$ RHE). Like most of NPCs, the T-FeNC-800R clearly exhibits much better methanol-tolerance ability than that of Pt/C. The ORR stability of T-FeNC-800R was tested with 10 000 cycles in the potential window of 0.6 to 1.0 V $vs.$ RHE at the scan rate of 50 mV s^{-1} on stationary electrode. After performing 10 000 stability test cycles, the $E_{1/2}$ of T-FeNC-800R exhibited a 61 mV negative potential shift, similar to the Pt/C (62 mV) (Fig. 5d), which suggested that the stability of the T-FeNC-800R was comparable to the Pt/C.

Conclusion

In this work, we have developed a high ORR active catalyst by pyrolysis the complex of Fe and bisPhen/6FDA using the SiO_2 nanoparticles as template. The pyrolysis temperature largely affected the ORR activity, and the optimal catalyst T-FeNC-800R pyrolyzed at 800 °C exhibited an excellent ORR activity under both alkaline and acidic conditions. The SiO_2 template played an important role on improving ORR activity via increasing the exposure of active sites of Fe-based catalysts and decreasing the diffusion resistance of ORR-relevant species (such as O_2 and H_2O). The second pyrolysis after HF leaching was also an important step to achieve high ORR performance. Moreover, compare with the commercial Pt/C, the T-FeNC-800R exhibited similar stability and much better methanol tolerance in acidic media. As a result, our as-prepared T-FeNC-800R catalyst is

a potentially viable alternative to precious Pt/C catalyst in PEMFCs with high ORR performance and superior stability.

References

1 S. Guo, S. Zhang and S. Sun, *Angew. Chem., Int. Ed.*, 2013, **52**, 8526–8544.

2 R. Borup, J. Meyers, B. Pivovar, Y. S. Kim, R. Mukundan, N. Garland, D. Myers, M. Wilson, F. Garzon, D. Wood, P. Zelenay, K. More, K. Stroh, T. Zawodzinski, J. Boncella, J. E. McGrath, M. Inaba, K. Miyatake, M. Hori, K. Ota, Z. Ogumi, S. Miyata, A. Nishikata, Z. Siroma, Y. Uchimoto, K. Yasuda, K.-i. Kimijima and N. Iwashita, *Chem. Rev.*, 2007, **107**, 3904–3951.

3 F. Jaouen, E. Proietti, M. Lefevre, R. Chenitz, J.-P. Dodelet, G. Wu, H. T. Chung, C. M. Johnston and P. Zelenay, *Energy Environ. Sci.*, 2011, **4**, 114–130.

4 A. Morozan, B. Jousselme and S. Palacin, *Energy Environ. Sci.*, 2011, **4**, 1238.

5 W. Xia, A. Mahmood, Z. Liang, R. Zou and S. Guo, *Angew. Chem., Int. Ed.*, 2016, **55**, 2650–2676.

6 B. C. H. Steele and A. Heinzel, *Nature*, 2001, **414**, 345–352.

7 M. Shao, Q. Chang, J.-P. Dodelet and R. Chenitz, *Chem. Rev.*, 2016, **116**, 3594–3657.

8 G. Wu, K. L. More, C. M. Johnston and P. Zelenay, *Science*, 2011, **332**, 443–447.

9 Y. Hu, J. O. Jensen, W. Zhang, L. N. Cleemann, W. Xing, N. J. Bjerrum and Q. Li, *Angew. Chem., Int. Ed.*, 2014, **53**, 3675–3679.

10 S. Guo and S. Sun, *J. Am. Chem. Soc.*, 2012, **134**, 2492–2495.

11 W. Wang, J. Luo, W. Chen, J. Li, W. Xing and S. Chen, *J. Mater. Chem. A*, 2016, **4**, 12768–12773.

12 D. Guo, R. Shibuya, C. Akiba, S. Saji, T. Kondo and J. Nakamura, *Science*, 2016, **351**, 361–365.

13 Z. Chen, D. Higgins, A. Yu, L. Zhang and J. Zhang, *Energy Environ. Sci.*, 2011, **4**, 3167–3192.

14 A. Serov, K. Artyushkova and P. Atanassov, *Adv. Energy Mater.*, 2014, **4**, 1301735.

15 M. Zhou, C. Yang and K.-Y. Chan, *Adv. Energy Mater.*, 2014, **4**, 1400840.

16 Z. K. Yang, Z.-W. Zhao, K. Liang, X. Zhou, C.-C. Shen, Y.-N. Liu, X. Wang and A.-W. Xu, *J. Mater. Chem. A*, 2016, **4**, 19037–19044.

17 A. Zitolo, V. Goellner, V. Armel, M.-T. Sougrati, T. Mineva, L. Stievano, E. Fonda and F. Jaouen, *Nat. Mater.*, 2015, **14**, 937–942.

18 F. Jaouen, S. Marcotte, J. P. Dodelet and G. Lindbergh, *J. Mater. Chem. B*, 2003, **107**, 1376–1386.

19 N. Ramaswamy, U. Tylus, Q. Jia and S. Mukerjee, *J. Am. Chem. Soc.*, 2013, **135**, 15443–15449.

20 M. Lefevre, E. Proietti, F. Jaouen and J. P. Dodelet, *Science*, 2009, **324**, 71–74.

21 W.-J. Jiang, L. Gu, L. Li, Y. Zhang, X. Zhang, L.-J. Zhang, J.-Q. Wang, J.-S. Hu, Z. Wei and L.-J. Wan, *J. Am. Chem. Soc.*, 2016, **138**, 3570–3578.

22 J. Masa, W. Xia, M. Muhler and W. Schuhmann, *Angew. Chem., Int. Ed.*, 2015, **54**, 10102–10120.

23 M. Eikerling, A. A. Kornyshev and A. R. Kucernak, *Phys. Today*, 2006, **59**, 38–44.

24 Z. Xia, L. An, P. Chen and D. Xia, *Adv. Energy Mater.*, 2016, **6**, 1600458.

25 H.-W. Liang, X. Zhuang, S. Bruller, X. Feng and K. Mullen, *Nat. Commun.*, 2014, **5**, 4973.

26 H.-W. Liang, W. Wei, Z.-S. Wu, X. Feng and K. Muellen, *J. Am. Chem. Soc.*, 2013, **135**, 16002–16005.

27 Y. Wang, A. Kong, X. Chen, Q. Lin and P. Feng, *ACS Catal.*, 2015, **5**, 3887–3893.

28 L. Lin, Q. Zhu and A.-W. Xu, *J. Am. Chem. Soc.*, 2014, **136**, 11027–11033.

29 L. Lin, Z. K. Yang, Y.-F. Jiang and A.-W. Xu, *ACS Catal.*, 2016, **6**, 4449–4454.

30 Z. K. Yang, L. Lin and A.-W. Xu, *Small*, 2016, **12**, 5710–5719.

31 S. Ji, H. Guo, X. Yuan, X. Li, H. Ding, P. Gao, C. Zhao, W. Wu, W. Wu and J. Zhao, *Org. Lett.*, 2010, **12**, 2876–2879.

32 S. J. Lee, S. S. Lee, M. S. Lah, J.-M. Hong and J. H. Jung, *Chem. Commun.*, 2006, 4539–4541.

33 W. Li, G. Chen, S. Zhang, H. Wang and D. Yan, *J. Polym. Sci., Part A: Polym. Chem.*, 2007, **45**, 3550–3561.

34 J. Jin, F. Pan, L. Jiang, X. Fu, A. Liang, Z. Wei, J. Zhang and G. Sun, *ACS Nano*, 2014, **8**, 3313–3321.

35 L. Zhao, Y. Wang and W. Li, *RSC Adv.*, 2016, **6**, 90076–90081.

36 J. Xue, L. Zhao, Z. Dou, Y. Yang, Y. Guan, Z. Zhu and L. Cui, *RSC Adv.*, 2016, **6**, 110820–110830.

37 A. Kong, X. Zhu, Z. Han, Y. Yu, Y. Zhang, B. Dong and Y. Shan, *ACS Catal.*, 2014, **4**, 1793–1800.

38 J. Shi, X. Zhou, P. Xu, J. Qiao, Z. Chen and Y. Liu, *Electrochim. Acta*, 2014, **145**, 259–269.

39 D. Shin, B. Jeong, B. S. Mun, H. Jeon, H.-J. Shin, J. Baik and J. Lee, *J. Phys. Chem. C*, 2013, **117**, 11619–11624.

40 Q. Z. Ren, J. W. Huang, Z. A. Zhu, L. N. Ji and Y. T. Chen, *J. Porphyrins Phthalocyanines*, 2001, **5**, 449–455.

41 F. Jaouen, M. Lefevre, J. P. Dodelet and M. Cai, *J. Mater. Chem. B*, 2006, **110**, 5553–5558.

42 F. Jaouen, J. Herranz, M. Lefevre, J.-P. Dodelet, U. I. Kramm, I. Herrmann, P. Bogdanoff, J. Maruyama, T. Nagaoka, A. Garsuch, J. R. Dahn, T. Olson, S. Pylypenko, P. Atanassov and E. A. Ustinov, *ACS Appl. Mater. Interfaces*, 2009, **1**, 1623–1639.

43 G. Wu, C. M. Johnston, N. H. Mack, K. Artyushkova, M. Ferrandon, M. Nelson, J. S. Lezama-Pacheco, S. D. Conradson, K. L. More, D. J. Myers and P. Zelenay, *J. Mater. Chem.*, 2011, **21**, 11392–11405.

44 Q. Wang, Z.-Y. Zhou, Y.-J. Lai, Y. You, J.-G. Liu, X.-L. Wu, E. Terefe, C. Chen, L. Song, M. Rauf, N. Tian and S.-G. Sun, *J. Am. Chem. Soc.*, 2014, **136**, 10882–10885.

45 L.-B. Lv, T.-N. Ye, L.-H. Gong, K.-X. Wang, J. Su, X.-H. Li and J.-S. Chen, *Chem. Mater.*, 2015, **27**, 544–549.

46 L.-T. Song, Z.-Y. Wu, F. Zhou, H.-W. Liang, Z.-Y. Yu and S.-H. Yu, *Small*, 2016, **12**, 6398–6406.

47 X. Zhou, Z. Bai, M. Wu, J. Qiao and Z. Chen, *J. Mater. Chem. A*, 2015, **3**, 3343–3350.